



JAAS

**High-Throughput Single-Pixel Spectral Imaging System For
Glow Discharge Optical Emission Spectrometry Elemental
Mapping Enabled by Compressed Sensing**

Journal:	<i>Journal of Analytical Atomic Spectrometry</i>
Manuscript ID	JA-ART-01-2022-000021.R1
Article Type:	Paper
Date Submitted by the Author:	17-Feb-2022
Complete List of Authors:	Gamez, Gerardo; Texas Tech University, Department of Chemistry and Biochemistry She, Yue; Texas Tech University, Department of Chemistry and Biochemistry Rivera, Paola; Texas Tech University, Department of Chemistry and Biochemistry Shi, Songyue; Texas Tech University, Department of Chemistry and Biochemistry Finch, Kevin; Texas Tech University, Department of Chemistry and Biochemistry

SCHOLARONE™
Manuscripts

1
2
3
4
5
6
7 **High-Throughput Single Pixel Spectral Imaging System For Glow Discharge Optical**
8
9 **Emission Spectrometry Elemental Mapping Enabled by Compressed Sensing**
10

11
12
13
14 Gerardo Gamez*, Yue She, Paola Rivera, Songyue Shi, Kevin Finch
15

16 Texas Tech University, Department of Chemistry and Biochemistry, Lubbock, TX 79409-41061,
17

18 USA. *Corresponding author. Phone: (806) 834-846 Email: gerardo.gamez@ttu.edu
19
20
21
22
23
24
25
26
27
28
29
30
31
32
33
34
35
36
37
38
39
40
41
42
43
44
45
46
47
48
49
50
51
52
53
54
55
56
57
58
59
60

Abstract

Glow discharge optical emission spectroscopy elemental mapping (GDOES EM), enabled by spectral imaging strategies, is an advantageous technique for direct multi-elemental analysis of solid samples in rapid timeframes. Here, a single-pixel, or point scan, spectral imaging system based on compressed sensing image sampling, is developed and optimized in terms of matrix density, compression factor, sparsifying basis, and reconstruction algorithm for coupling with GDOES EM. It is shown that a 512 matrix density at a compression factor of 30% provides the highest spatial fidelity in terms of the peak signal-to-noise ratio (PSNR) and complex wavelet structural similarity index measure (cw-SSIM) while maintaining fast measurement times. The background equivalent concentration (BEC) of Cu I at 510.5 nm is improved when implementing the discrete wavelet transform (DWT) sparsifying basis and Two-step Iterative Shrinking/Thresholding Algorithm for Linear Inverse Problems (TwIST) reconstruction algorithm. Utilizing these optimum conditions, a GDOES EM of a flexible, etched-copper circuit board was then successfully demonstrated with the compressed sensing single-pixel spectral imaging system (CSSPIS). The newly developed CSSPIS allows taking advantage of the significant cost-efficiency of point-scanning approaches (>10x vs intensified array detector systems), while overcoming (up to several orders of magnitude) their inherent and substantial throughput limitations. Ultimately, it has the potential to be implemented on readily available commercial GDOES instruments by adapting the collection optics.

1. Introduction

Mapping the distribution of elements in solid samples is critical for understanding the underlying mechanisms of natural and engineered materials¹⁻⁷. There are several elemental mapping (EM) techniques currently available but, while they possess different advantages, a common limitation is long acquisition times, which can require several hours or more. Glow discharge optical emission spectroscopy (GDOES) has been shown to permit EM from within the sputtered area when operated in pulsed power mode and sustained under higher-than-typical pressures⁸⁻¹⁵. Leveraging the inherent GDOES advantages of direct solid sampling, simultaneous multi-elemental analysis, fast sputtering rates, multi-matrix calibration schemes, and depth profiling in the nm scale, results in ultra-high throughput elemental mapping capabilities that can be several orders-of-magnitude faster vs typical techniques^{2, 11, 16}.

One of the aspects that enables GDOES EM is its coupling to an appropriate spectral imaging system for data collection, with several embodiments reported. On the one hand, wavelength-scan approaches, also known as staring-camera type, allow measuring monochromatic images one wavelength at a time, with the advantage of giving access to both spatial dimensions simultaneously. The wavelength selection device used influences greatly the GDOES EM performance: a monochromator gives access to a wide λ range but λ -scan is slow and it compromises light-throughput vs. spectral resolution^{8,9}; a dichroic filter is very cost effective and can have a large numerical aperture (NA) but the λ range and spectral resolution for each filter are very limited, such that tens of filters would be needed for multi-elemental analysis¹⁴; acousto-optic tunable filters give fast random λ access and can also have a large NA but they have limited λ range and UV capabilities, spectral resolution that varies with λ , and can be costly¹⁵. On the other hand, line-scan approaches, also known as push-broom type, allow measuring

1
2
3 one spatial dimension and the λ dimension simultaneously while the remaining spatial dimension
4
5 has to be scanned. Reported grating spectrograph line-scan systems used for GDOES EM have
6
7 shown large NA, a wide λ range that could potentially be extended into VUV, and fast
8
9 hyperspectral imaging capabilities¹⁰⁻¹³. One type of spectral imaging system that has not yet
10
11 been demonstrated with GDOES EM is the point-scan approach, or single-pixel imaging system
12
13 (SPIS). The main reason is that the typically required scanning in the two spatial dimensions
14
15 leads to significantly slower data acquisition. However, the use of a single pixel detector is the
16
17 most hardware cost-effective approach, by at least an order of magnitude, in contrast to the 2D
18
19 array detectors necessary for GDOES EM with the line- or wavelength-scanning approaches.
20
21
22

23
24 Compressed sensing (CS) is a sampling scheme that allows reconstruction of signals with
25
26 only a fraction of the samples required by the Nyquist theorem, thus allowing for much faster
27
28 data acquisition¹⁷⁻²⁷. The principles that enable CS are: group sampling, which allows obtaining
29
30 more information per sample and inherent multiplex advantages; incoherence, which translates
31
32 into random selection of groups for sampling to avoid bias and improve the probability of
33
34 including all required components in less measurements; and data sparsity, which refers to
35
36 having most of the signal information contained in only a few components, or ample redundant
37
38 information, such that the data is compressible. Thus, several CS based approaches have been
39
40 demonstrated for allowing much faster data acquisition in single-pixel imaging systems²⁸⁻³⁴.
41
42
43

44
45 Herein, a CSSPIS, based on a digital micromirror device (DMD) spatial modulator, is
46
47 developed and adapted for GDOES EM. The effects of the operating and image reconstruction
48
49 parameters are studied with respect to the image fidelity performance and the optimized
50
51 operating conditions are demonstrated with GDOES EM. This will enable taking advantage of
52
53 the SPIS significant cost-effectiveness and make GDOES EM more accessible, while allowing
54
55
56
57
58
59
60

1
2
3 for much faster throughput compared to its traditional SPIS counterpart. An additional potential
4 advantage is that this approach opens the possibility to perform EM on commercial GDOES
5 systems, typically featuring single-pixel detectors, by adapting the optical collection path with a
6 spatial modulator.
7
8
9
10

11 **2. Experimental**

12 **Compressed Sensing Single Pixel Spectral Imaging System**

13
14
15 The GD lamp, previously described in ⁹, was adapted with a 9 mm cathode sputtering
16 diameter. The GD was operated under UHP Ar gas (99.999%) flowing at a rate of 0.15 L/min
17 controlled by a mass flow controller (Apex, AX-MC-1SLPM-D/5M) and in conjunction with a
18 roughing pump (Edwards, RV12), resulted in a pressure of 14 Torr monitored by a pressure
19 gauge (MKS, 901P-11040). The RF power supply (Dressler, Cesar 1350) was pulsed at 1 kHz
20 and 4% duty cycle, and the forward power was adjusted to ~350 W with the reflected power <5
21 W. A chiller (Thermo Scientific, Neslab Merlin M25) cooled the RF power supply, impedance
22 matching network, and GD backing electrode.
23
24
25
26
27
28
29
30
31
32
33
34

35 Figure 1A shows how the light from the GD was collected with a series of plano-convex
36 singlet lenses (Thorlabs, fused silica, 2 inch diameter, 200 mm focal length). L1 collimates the
37 light towards a flat dielectric mirror (Thorlabs, fused silica, BB3-E02) that reflects it to L2,
38 which focuses the light onto the DMD (Texas Instruments, DLP® LightCrafter™ Evaluation
39 Module with DLP 0.3 WVGA chipset). L3 then collimates the encoded light from the DMD and
40 L4 focuses the light onto the entrance slit of the monochromator (Chromex, Model 500iS/SM,
41 linear dispersion 1.6 nm/mm), which was open to the maximum width of 2 mm. The exit slit
42 width was also completely open to 2 mm and a PMT (Hamamatsu, R928P), connected to a high
43 voltage power supply (Bertan, 230-05R), was used for detection.
44
45
46
47
48
49
50
51
52
53
54
55
56
57
58
59
60

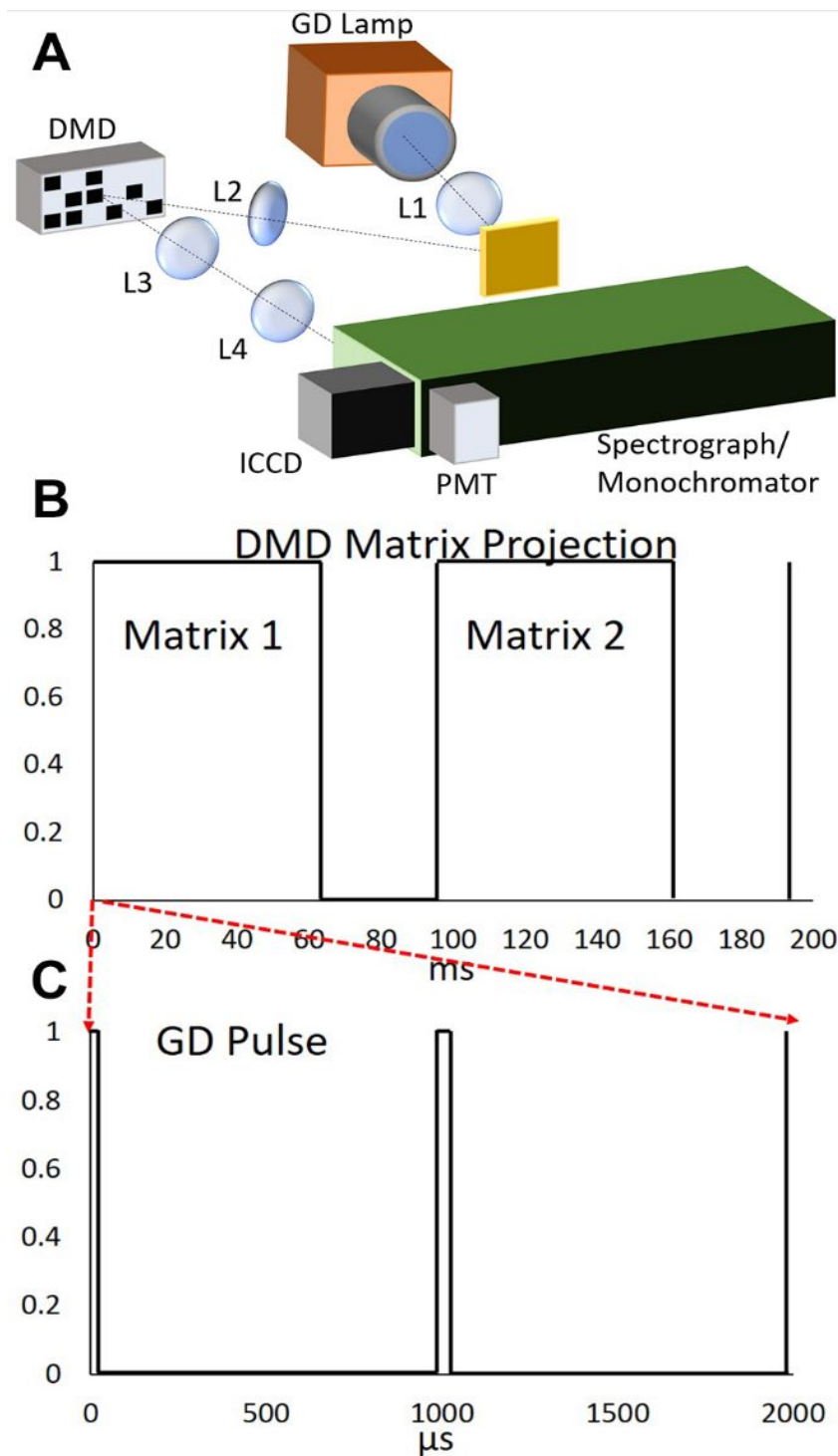


Figure 1. A) Schematic of the instrument setup for CSSPIS from GDOES EM where the light is imaged onto the DMD spatial modulator and the resulting encoded image is refocused into the monochromator. B) The experimental timing showing the DMD projection period and the GD pulsing frequency. Note the different time scales of each plot. See Experimental section for further details.

The PMT output was split in two with the first part connected to a low noise amplifier (Stanford

1
2
3 Research Systems, Model SR570) followed by a low-pass filter (KROHN-HITE, Model 3342)
4 and digitized by DAQ (National Instruments, USB-6259), while the second part was connected
5
6 to a home-built amplifier and digitized by another DAQ (National Instruments, USB-6001). The
7
8 purpose of this was for measuring the full dynamic range with a low-gain branch, which is
9
10 advantageous for measuring the baseline and the highest intensities resulting from just a few
11
12 selected encoding masks, i.e. matrices. However, most of the matrices will yield similar
13
14 intensities, thus using the high-gain branch allows “zooming-in” around these intensities and
15
16 enables to better distinguish the differences that contain most of the information, but the few
17
18 highest intensity data will be appear saturated in this case.
19
20
21
22
23

24 **Image Encoding**

25
26 Figure 1B&C show the experimental timing diagram. The DMD was setup as a second
27
28 monitor to a computer, such that it projected a video consisting of a sequence of encoding
29
30 matrices. These video sequences of Scrambled Block Hadamard Ensemble (SBHE) structurally
31
32 random matrices (SRM) were produced as previously described²⁸. Different video sequences
33
34 were produced at various matrix densities, including 512, 1024, 2048, and 4096. In short, the
35
36 image size is 256 x 256 pixels, for a total of 65536 pixels. The matrix density refers to number of
37
38 DMD pixels that simultaneously reflect parts of the image towards the detector, where their
39
40 respective intensities are combined. In addition, video sequences at different compression factors
41
42 were also produced, including 10%, 20%, 30%, 40%, 50%, and 100%. The compression factor
43
44 refers to the fraction of measurements/combinations used to reconstruct the image with respect to
45
46 the ones required by the Nyquist theorem, or in a determined system of equations, which would
47
48 correspond to 65536 for 100% in our case. During all video sequences, each different encoding
49
50 matrix was projected (ON) for ~66 ms, followed by a blank matrix (OFF) projected for ~33 ms
51
52
53
54
55
56
57
58
59
60

1
2
3 that served to block the GD emission from reaching the monochromator. This effectively results
4
5 in a sequence of baseline resolved intensity peaks that enable improved analysis and processing
6
7 of GDOES intensity data collected for each matrix ²⁸.
8
9

10 **Data Analysis**

11
12 The data analysis and processing consists of several steps. Essentially, the intensity of each
13
14 matrix combination is averaged over its ON time and extracted into a single file. Next, the low-
15
16 gain and high-gain intensity data are combined by matching the different scales, which allows
17
18 replacing the saturated intensities in the high-gain data set with the unsaturated ones in the low-
19
20 gain set. Then, if necessary, baseline and amplitude drift corrections are applied, where a small
21
22 set of identical encoding matrices, applied before the beginning and after the end of the
23
24 measurement, are used to assess the drift. Finally, two CS algorithms, selected for their speed
25
26 advantages ³⁵, were implemented for image reconstruction, including Two-step Iterative
27
28 Shrinking/ Thresholding Algorithm for Linear Inverse Problems (TwIST) ³⁶ and Gradient
29
30 Projection for Sparse Reconstruction (GPSR) ³⁷. In addition, two different sparsifying basis,
31
32 including 9-7 discrete wavelet transform (DWT) and discrete cosine transform (DCT), were
33
34 utilized. The reconstructed images were median filtered (12x12 block size) and the intensity
35
36 scale normalized to 16 bit.
37
38
39
40
41

42 **3. Results & discussion**

43
44
45 The model sample used for studying the effect of the operating/reconstruction conditions on
46
47 GDOES EM CSSPIS was a nickel (75.2%)/chromium (19.4%) alloy substrate (NIMONIC alloy
48
49 75, E3918, 0.005% copper) with pure copper wire surface inserts of 1 mm diameter, separated by
50
51 1 mm edge-to-edge (Figure 2A). Figure 2B shows an end-on picture of the sample in the
52
53
54
55
56
57
58
59
60

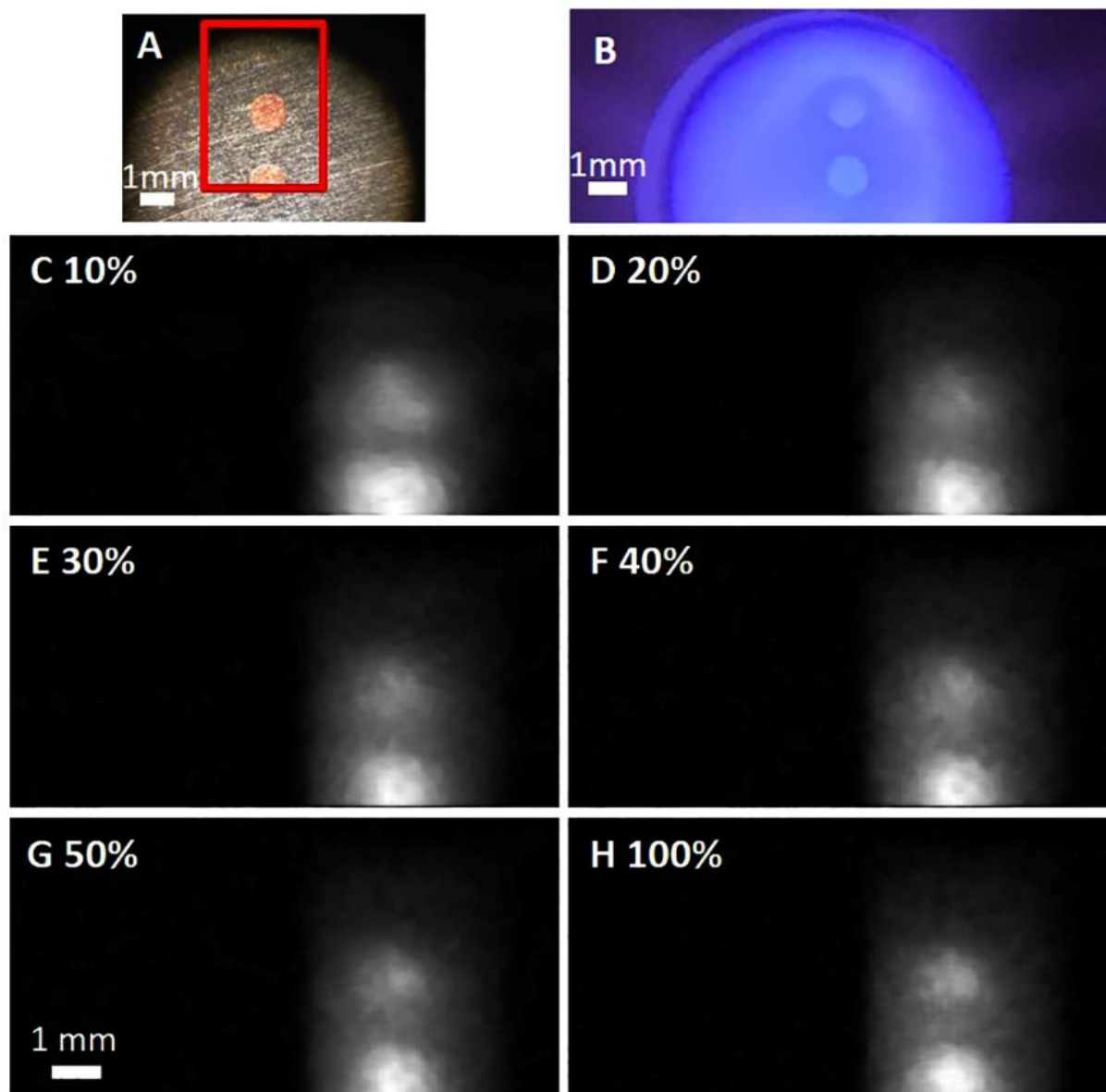


Figure 2. A) Model sample of stainless steel SRM with pure copper inserts. B) End-on view of mounted model sample during GD operation (plasma ON). C-H) Reconstructed images obtained with the CSSPIS from GDOES EM of the model sample at 510.5 nm, Cu I, under different compression factors (matrix density 512, DWT, TwIST).

chamber while the GD is in operation (plasma ON). Given the slit width limitations of the monochromator, only part of the GDOES image projected on to the DMD made it through to the PMT detector, which is highlighted by the red rectangle in Figure. 2A. Figures 2C to 2H show

1
2
3 samples of reconstructed spectral images under selected conditions. It is evident that the image
4
5 quality improves as more measurements are obtained, or at higher compression factor
6
7 percentages, particularly from 10% to 30% while higher percentages yield diminishing returns.
8
9

10 **Fidelity Assessment**

11
12
13 The fidelity of the spectral images obtained with the CSSPIS was quantified by two methods:
14
15 the more typical peak signal-to-noise ratio (PSNR) method and the complex wavelet structural
16
17 similarity index measure (cw-SSIM). The PSNR method calculates the mean squared error
18
19 (MSE) by doing a pixel-to-pixel comparison between the image of interest and a standard image.
20
21 This is followed by weighing the MSE with the maximum possible pixel value and expressing
22
23 the result in decibels, where higher PSNR values indicate improved fidelity. While the PSNR
24
25 metric has several advantages, including that is simple to compute, it is a global measure that is
26
27 not very well suited to assess perceived visual quality³⁸. For example, the PSNR value will be
28
29 significantly affected if the image of interest is exactly the same as the standard image but just
30
31 shifted a couple of pixels.
32
33
34
35
36

37
38 The SSIM method is a slightly more involved calculation but gives a better assessment of
39
40 perceived visual quality^{38,39}. In this case, the interdependency of nearby pixels is taken into
41
42 account by only focusing on a small window section, or local group of pixels, of the image-of-
43
44 interest (x) and the corresponding one in the standard image (y) at any given time. It compares
45
46 luminance (l , or brightness, measured as the average intensity, μ), contrast (c , measured as
47
48 standard deviation, σ), and structure (s , measured as cross correlation of x and y after mean
49
50 removal, σ_{xy}) between the small image sections³⁸:
51
52
53
54
55
56
57
58
59
60

$$S(x,y) = l(x,y) \cdot c(x,y) \cdot s(x,y) = \left(\frac{2\mu_x\mu_y + C_1}{\mu_x^2 + \mu_y^2 + C_1} \right) \cdot \left(\frac{2\sigma_x\sigma_y + C_2}{\sigma_x^2 + \sigma_y^2 + C_2} \right) \cdot \left(\frac{2\sigma_{xy} + C_3}{\sigma_x\sigma_y + C_3} \right)$$

where C_1 , C_2 and C_3 are small positive constants to stabilize near zero values. The small window section is then shifted pixel-by-pixel across the image to yield an SSIM map and the total SSIM score is obtained by averaging all the SSIM map values. The total SSIM values are expressed in a zero to 1 scale, where values closer to 1 indicate higher fidelity.

The results of the fidelity assessment for the 512 matrix density as a function of compression factor are shown in Figure 3. It should be noted that only the part of the image that made it through the monochromator entrance slit (brighter part of Figures 2C-H, corresponding to the red box highlight of Figure. 2A) was taken into account for the comparison. In general, the PSNR values improve from ~28db at 10% compression factor to ~32db at 30%. On the other hand, the PSNR stays constant from 30% to 50% compression factor. The SSIM shows a similar trend, with values improving from ~0.85 at 10% to ~0.9 at 30%, where they reach a plateau.

Interestingly, the effect of the algorithm, or sparsifying basis, used during the reconstruction is indistinguishable within the experimental error for both fidelity quantification methods. These general trends change gradually as the matrix density is increased to 1024 (Figure. S1), 2048 (Figure. S2), and ultimately 4096 (Figure. 4). For example, the PSNR values keep increasing as a function of compression factor, with no evident plateau, and with a steeper slope at higher matrix densities. Furthermore, the overall PSNR values obtained are worse as the matrix density is increased, particularly at lower compression factors. It is also worth noting that the choice of sparsifying basis and reconstruction algorithm start to have an increasingly significant effect at higher matrix densities.

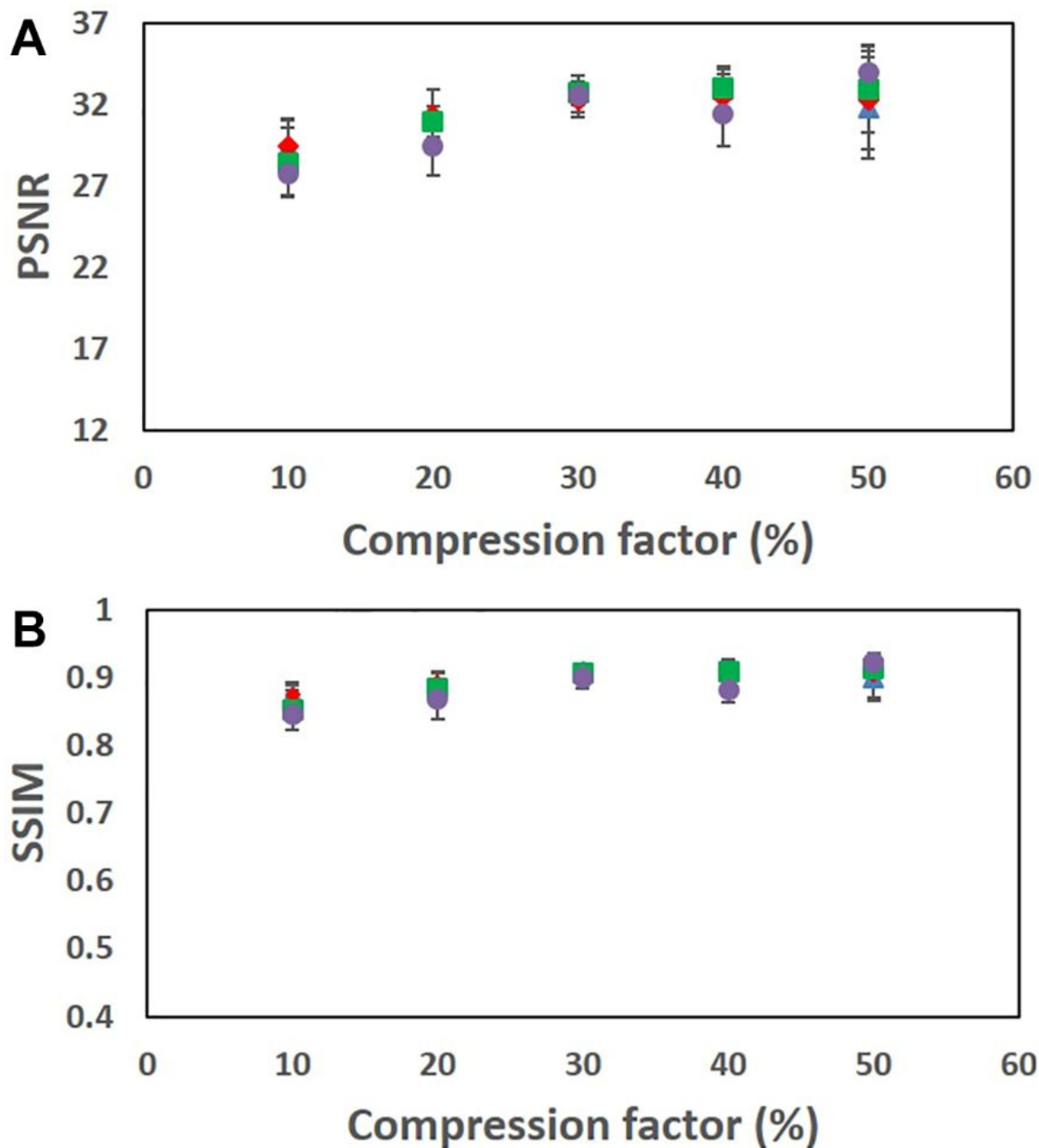


Figure 3. Fidelity characterization, in terms of PSNR (A) and SSIM (B), of GDOES EM CSSPIS reconstructed images at 512 matrix density as a function of compression factor. The effect of the sparsifying basis/reconstruction algorithm were also studied: DCT/TwIST (♦), DWT/TwIST (●), DCT/GPSR (▲), DWT/GPSR (■).

1
2
3 The GPSR algorithm, as well as DCT sparsifying basis, performs better at lower compression
4 factors and increased matrix densities. This is particularly evident at 4096 (Figure. 4) where a
5 paired data t-test (2-tail, significance = 0.05) including all compression factors gives a p-value of
6 1.6×10^{-3} for DCT and 1.1×10^{-3} for DWT, to confirm GPSR outperforms TwIST. In addition,
7 when GPSR is used, DCT outperforms DWT (p-value 1.8×10^{-2}). On the other hand, the effect of
8 algorithm and basis starts to once again become indistinguishable when the number of
9 measurements is increased to 50% compression factor. It is instructive to see that the visual
10 perception-based SSIM at 4096 matrix density shows a similar trend. The better performance of
11 GPSR vs TwIST is more evident here (p-values of 9.2×10^{-6} for DCT, and 3.1×10^{-5} for DWT), but
12 DCT outperforms DWT only up to 30% compression factor (p-values of 1.3×10^{-2} for GPSR, and
13 1.5×10^{-3} for TwIST), which also put into perspective the more abstract PSNR values.

14
15
16
17
18
19
20
21
22
23
24
25
26
27
28
29 The better performance of the 512 matrix density has to do with the corresponding matrix
30 signal and its precision. As mentioned above, the matrices, or encoding masks, displayed on the
31 DMD enable combining the intensities of several parts of the image at the PMT detector. Each
32 matrix is a different combination so it is critical to be able to distinguish between the different
33 resulting intensities. When less parts of the image are combined (512 matrix density) the
34 differences between the corresponding matrix measured intensities are larger, such that it is
35 easier to distinguish the differences under a particular set of signal and standard deviation
36 conditions. As more parts of the image are combined (up to 4096 matrix density) the differences
37 become gradually smaller, such that the inherent signal and noise conditions play a more
38 important role, thus making them harder to distinguish.
39
40
41
42
43
44
45
46
47
48
49
50
51
52
53
54
55
56
57
58
59
60

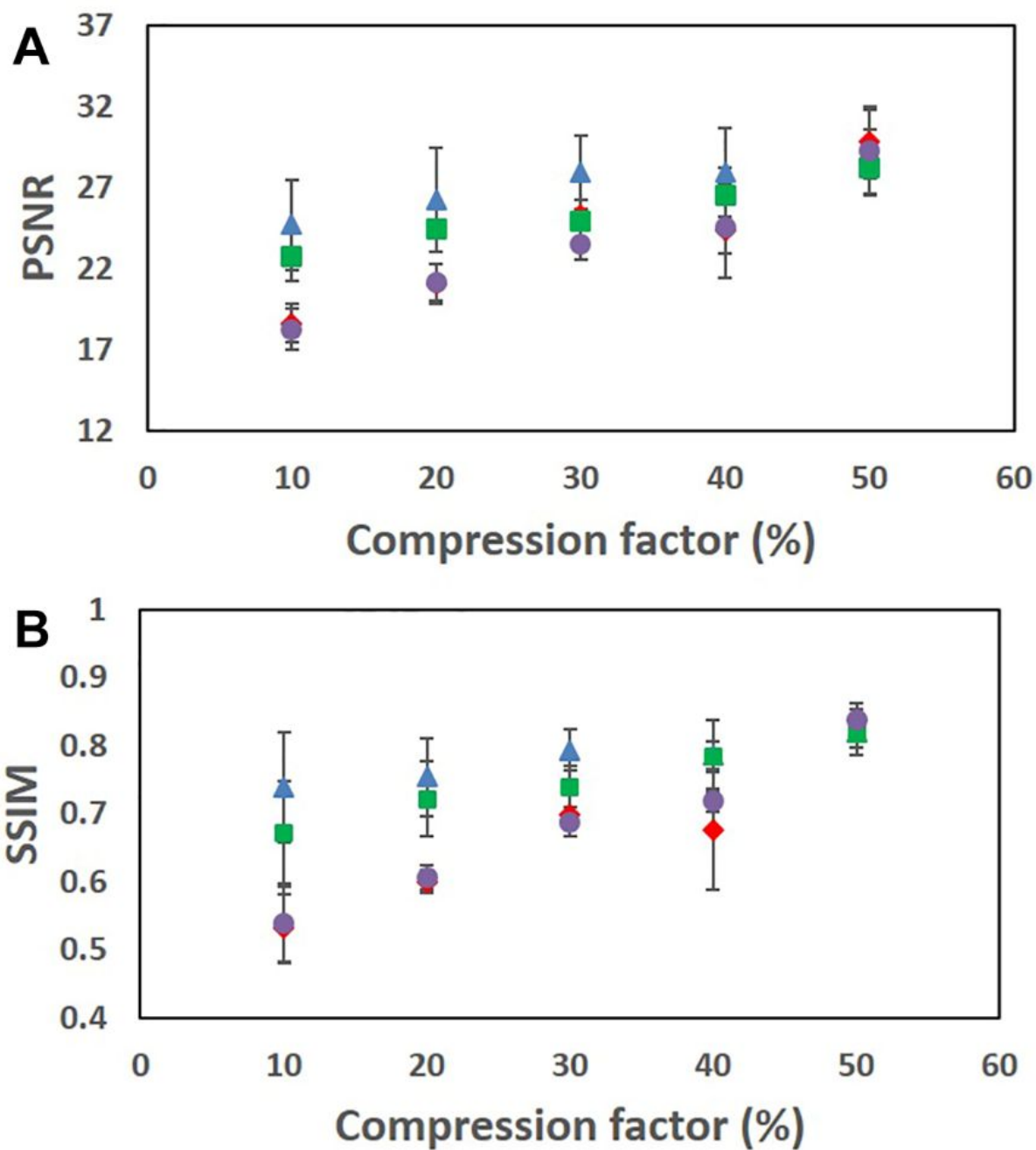


Figure 4. Fidelity characterization, in terms of PSNR (A) and SSIM (B), of GDOES EM CSSPIS reconstructed images at 4096 matrix density as a function of compression factor. The effect of the sparsifying basis/reconstruction algorithm were also studied: DCT/TwIST (♦), DWT/TwIST (●), DCT/GPSR (▲), DWT/GPSR (■).

Of course, there is a compromise between matrix intensity differences and the brightness of the light source being studied. For example, under very low light level conditions the overall signal-

1
2
3 to-noise (SNR) level from the combinations coming from the smaller density matrices may start
4
5 to become inadequate, leading to worse performance compared to higher matrix densities, as
6
7 shown in ²⁸.
8
9

10
11 Computer simulations of the CSSPIS process were performed to better understand the
12
13 observed trends. In this case, the CameraMan image was used and noise was added with the
14
15 MATLAB function “awgn” (adds white Gaussian noise to signal) at a ratio of signal power to
16
17 noise power of 50 dBW, thus simulating source noise (Figure S3). The image was multiplied
18
19 sequentially by each matrix (binary, 1 and 0) in the corresponding series, and the pixel values in
20
21 each resulting image were integrated. This was followed by the image reconstruction method
22
23 described in the *Data Analysis* section above. Figures 5 (512 matrix density) and 6 (4096 matrix
24
25 density), as well as S4 (1024) and S5 (2048), show the PSNR and SSIM as a function of
26
27 compression factor for the simulation experiments. While the absolute PSNR and SSIM values
28
29 are not comparable, the trends are very instructive. For example, there is a general improved
30
31 performance with increased percentages, which is consistent with the experimental data. Also,
32
33 the performance of the 512 matrix density, as evidenced by the higher PSNR and SSIM values, is
34
35 better compared to the 4096 matrix. This is again consistent with the experimental data. The
36
37 trends with respect to effect of the reconstruction algorithm or sparsifying basis are not the same,
38
39 which may be due to the experimental data containing both source and detector noise, while the
40
41 simulated data only has source noise added.
42
43
44
45
46
47
48
49
50
51
52
53
54
55
56
57
58
59
60

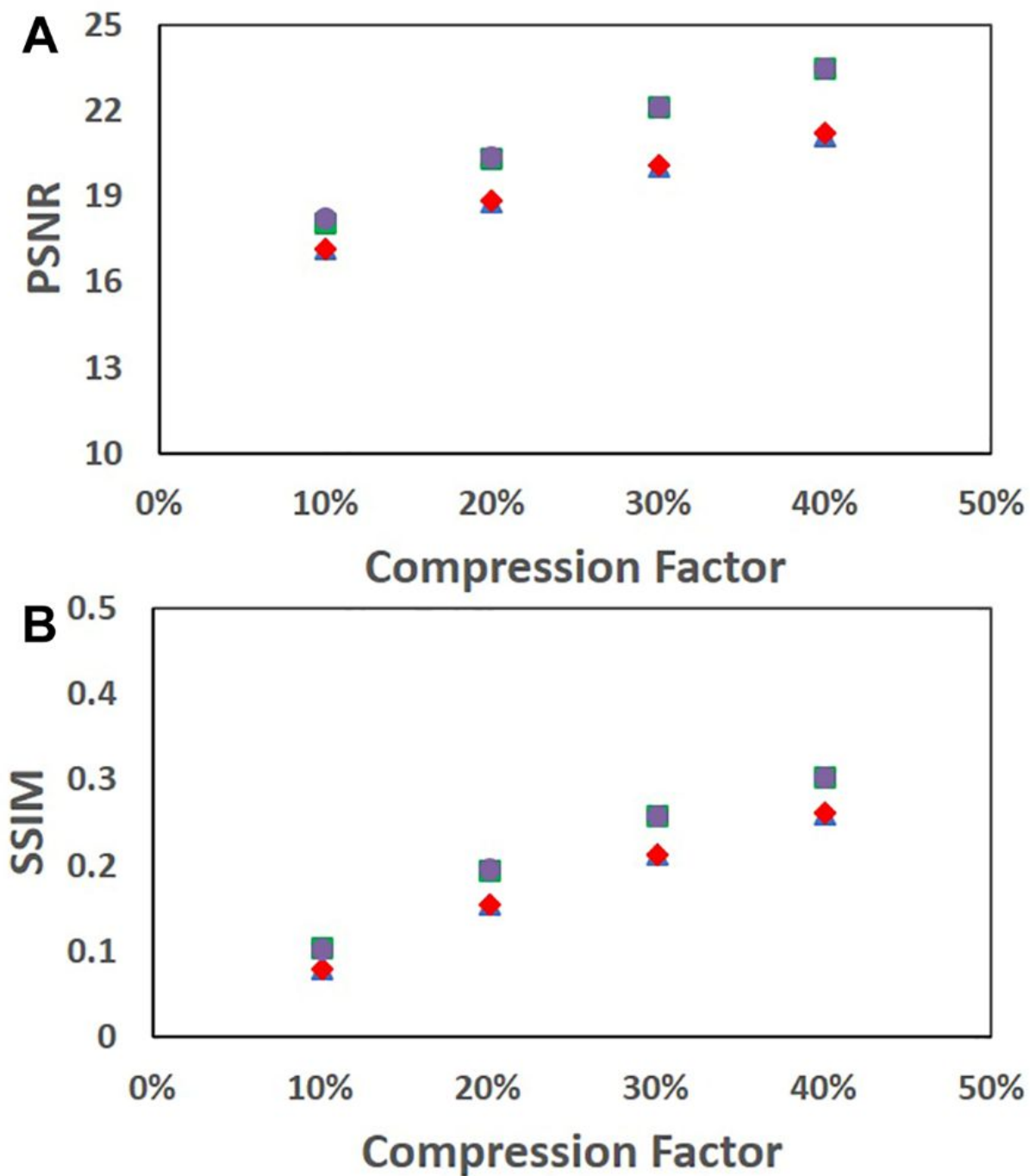


Figure 5. Fidelity characterization, in terms of PSNR (A) and SSIM (B), of computer simulated CSSPIS reconstructed images at 512 matrix density as a function of compression factor. The effect of the sparsifying basis/reconstruction algorithm were also studied: DCT/TwIST (♦), DWT/TwIST (●), DCT/GPSR (▲), DWT/GPSR (■).

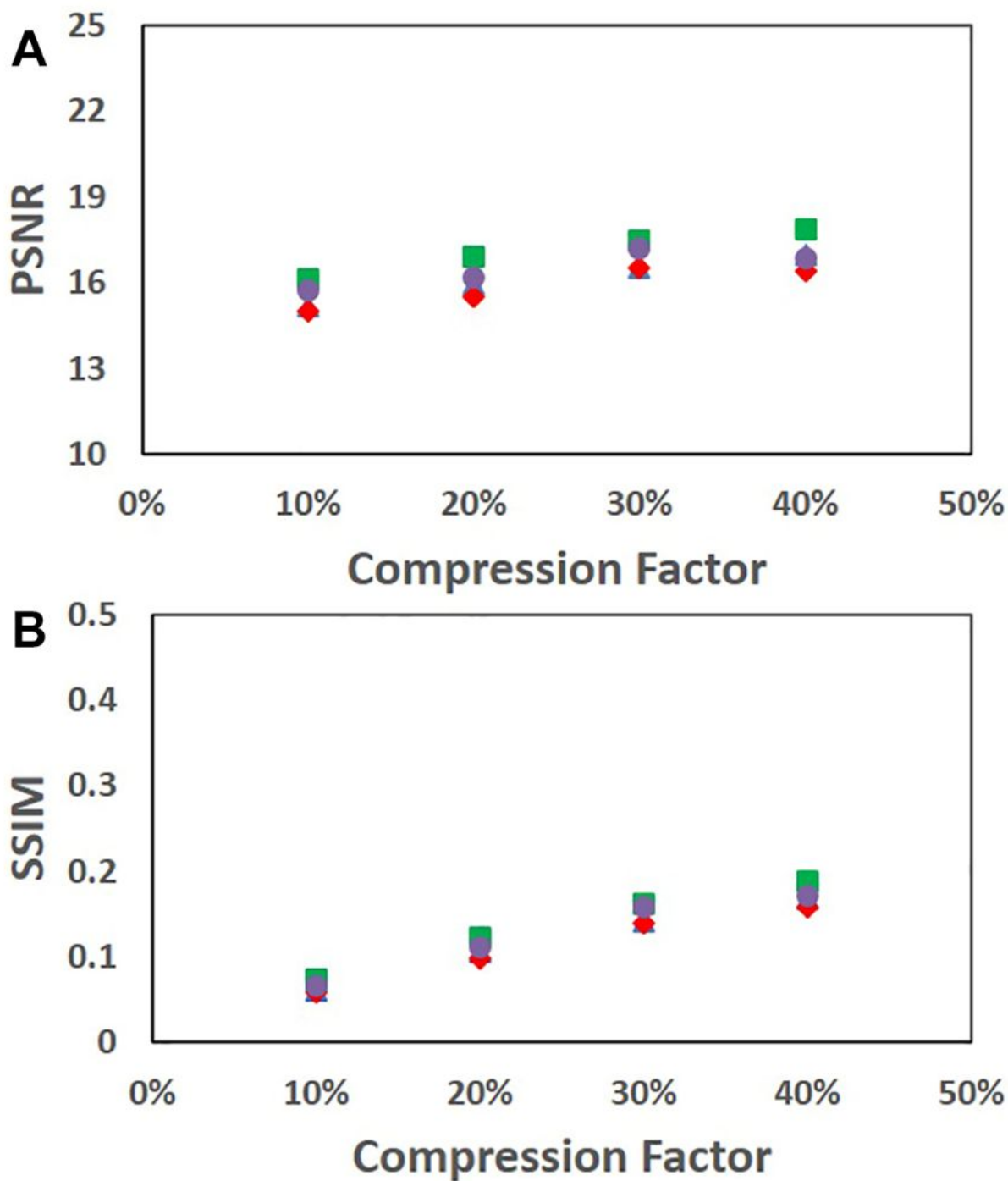


Figure 6. Fidelity characterization, in terms of PSNR (A) and SSIM (B), of computer simulated CSSPIS reconstructed images at 4096 matrix density as a function of compression factor. The effect of the sparsifying basis/reconstruction algorithm were also studied: DCT/TwIST (◆), DWT/TwIST (●), DCT/GPSR (▲), DWT/GPSR (■).

An important aspect to consider is how these parameters would affect the quantitative elemental analysis. Thus, the images reconstructed from the data obtained with the optimum 512 matrix density were used to calculate background equivalent concentrations (BEC), of the copper inserts (Figure 7):

$$BEC = \frac{0.01 \times k \times RSDB \times C_0}{SBR}$$

where the constant $k = 3$, RSDB is the relative standard deviation of the background, SBR is the signal to background ratio, and C_0 is the copper insert concentration at 99%. The signal was averaged over the copper insert area, while the background was averaged over a comparable area on the substrate.

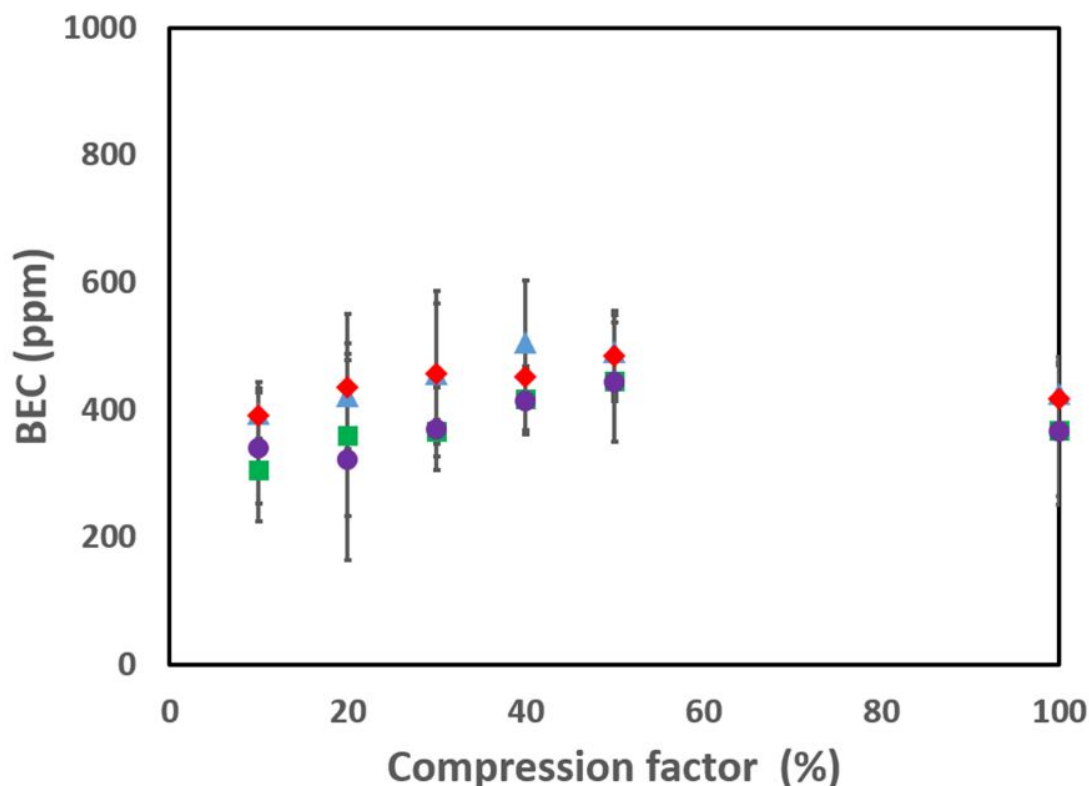


Figure 7. Background equivalent concentration (BEC) of copper (Cu I, 510.5 nm) from GDOES EM CSSPIS reconstructed images of the model sample at 512 matrix density as a function of compression factor. The effect of the sparsifying basis/reconstruction algorithm were also studied: DCT/TwIST (◆), DWT/TwIST (●), DCT/GPSR (▲), DWT/GPSR (■).

1
2
3 It is interesting to note that in general the BEC value increases, or becomes worse, from 10%
4 compression factor compared to 40% (p-value 3.3×10^{-3}). This trend can be explained by looking
5 at Figure. 1, where the images recovered at 10% look smoothed, or blurred, compared to 40%,
6 which results in lower RSDB values and translates into a lower BEC at 10%. The BEC decreases
7 again when comparing 40% to 100% (p-value 2.8×10^{-2}), but this is due to higher SBR at 100%.
8 In addition, DWT gives better, or lower, BECs compared to DCT (paired data t-test, 2 tail,
9 including all compression factors) with p-values of 2.2×10^{-5} for GPSR, and 3.9×10^{-4} for TwIST.
10 The BEC values are estimates of detection limits and here they are one to two orders of
11 magnitude higher compared to typical ones reported for GDOES bulk analysis, due to several
12 factors. First, the use of higher operating pressures here leads to lower sputtering rates and
13 corresponding lower emission signals. Nonetheless, this change is expected to be less than an
14 order of magnitude. Second, and most important, the detection limits in bulk analysis are
15 achieved by integrating the signal for up to 10 s under continuous GD power. On the other hand,
16 the PMT here was allowed to collect light for ~ 0.066 s during each matrix measured. However,
17 the GD power is pulsed at 1 kHz with a 4% duty cycle, which lowers the time the GD signal is
18 actually collected to 0.00264 s per matrix. Furthermore, one has to take into account the number
19 of times the same DMD pixel is included in the total measurement, which comes out to ~ 154 by
20 using the matrix density (512), image pixel density (256 x 256) and compression factor (0.3).
21 Thus, the total time in which signal is collected per pixel in the complete measurement here is
22 ~ 0.4 s, compared to the 10 s typically used for bulk analysis, which helps to explain the
23 difference in detection limits, together with the lower sputtering rates at the higher pressures. A
24 similar effect on detection limits is observed when performing GDOES depth profiling studies
25 where the signal is integrated for much shorter times, ~ 0.1 s, compared to bulk analysis.
26
27
28
29
30
31
32
33
34
35
36
37
38
39
40
41
42
43
44
45
46
47
48
49
50
51
52
53
54
55
56
57
58
59
60

1
2
3 Finally, GDOES EM of a flexible, etched-copper board sample was successfully demonstrated
4 with the optimized CSSPIS (Figure 8). A matrix density of 512 was implemented because it
5 proved to be optimum in terms of spatial fidelity at the lower 30% compression factor to permit
6 the fastest measurement. Also, the DWT sparsifying basis and TwIST reconstruction algorithm
7 were used because they showed better BEC values. The CSSPIS measurement is significantly
8 faster compared to typical SPIS systems relying on pixel-to-pixel rastering. In fact, the improved
9 measurement time is not linear, as the 30% value would suggest, because the intensities from
10 many pixels, 512 in this case, are combined at any given measurement. This multiplexing yields
11 a significant improvement in SNR ratio at the detector compared to single pixel rastering systems
12 and provides for considerably faster data acquisition times. The enhancement would correspond
13 to the improvement in SNR, which is \sim equivalent to the number of combined pixels (more than
14 two orders-of-magnitude), when the noise is detector limited. The actual measurement time for
15 the data shown in Fig. 8 is \sim 32 min, which is already competitive with other elemental mapping
16 techniques. On the other hand, it is at least an order of magnitude slower compared to the time
17 required by GDOES EM using line- or wavelength-scan spectral imaging techniques. However,
18 the current measurement time here is limited by implementing the DMD as a second monitor
19 (and corresponding relatively-slow refresh rate), the pulsed GD power duty cycle, and the signal
20 averaging during the time the matrix is projected, which results in a “dilution” of 4% signal in
21 96% background. Uploading shorter matrix series directly into the limited DMD memory would
22 permit much faster refresh rates and to implement DMD-based synchronized detection strategies,
23 as demonstrated for LIBS⁴⁰, making the current matrix OFF-time unnecessary and enabling a
24 significantly improved SBR and lateral resolution⁹. Such improvements would allow
25 significantly faster acquisition times at similar LODs or better LODs at similar acquisition times.
26
27
28
29
30
31
32
33
34
35
36
37
38
39
40
41
42
43
44
45
46
47
48
49
50
51
52
53
54
55
56
57
58
59
60

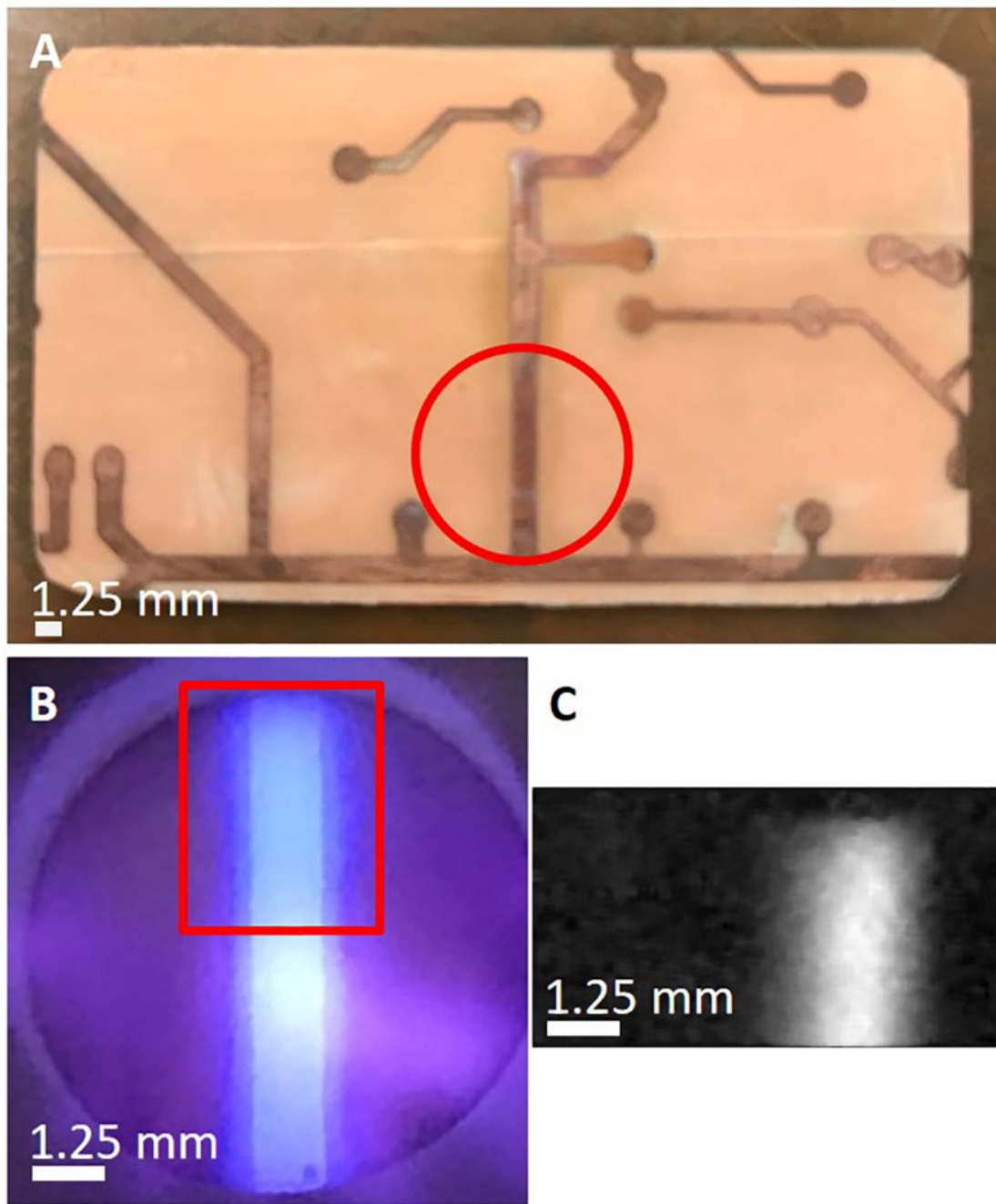


Figure 8. A) Etched copper flexible electrical board sample, with red circle showing area samples by GD. B) End-on view of mounted copper-board sample during GD operation, with red rectangle showing area imaged by the CSSPIS. C) GDOES EM of copper (Cu I, 510.5 nm) with CSSPIS under optimized conditions of 512 matrix density, 30% compression factor, DWT sparsifying basis, and TwIST reconstruction algorithm.

4. Conclusions

A CSSPIS has been tailored and implemented to GDOES EM for the first time, with optimization from actual GD plasma emission. In terms of spatial fidelity, the addition of a SSIM assessment to the PSNR has allowed a better understanding of the reconstructed images in terms of visual perception. The best fidelity performance displayed by the 512 matrix density can be attributed to the greater differences in peak intensity measured for each of the encoded matrices, where a compression factor of 30% already yields optimum results. The quantitative performance, in terms of BEC, shows the DWT sparsifying basis and TwIST reconstruction algorithm to be best.

Under optimized conditions, the CSSPIS approach can be significantly faster (orders of magnitude in detector noise limited cases) than the traditional pixel-by-pixel scanning counterpart because of the compression and multiplexing properties. Furthermore, while the measurements here were performed under non-gated continuous detection, DMDs have the potential to allow synchronized gated detection of pulsed plasmas with high temporal resolution, as demonstrated for LIBS⁴⁰, which would lead to improved SBR and lateral resolution in GDOES EM⁹. Ultimately, the CSSPIS strategy is also amenable for being adapted to a potential implementation on readily available commercial GDOES instruments to allow multi-EM capabilities.

It is worth noting that array detectors can make CS spectral imaging approaches much more powerful by allowing many combinations to be measured at the same time and having simultaneous access to the wavelength dimension, which results in much faster imaging with multi-elemental capabilities. Thus, current work in the PI lab is already underway to incorporate

an array detector and enable coded aperture snapshot spectral imaging (CASSI)^{19, 41} with the ultimate capability of capturing a full hyperspectral data cube in a single snapshot.

5. Acknowledgments

The authors would like to acknowledge support by the National Science Foundation under CHE-1610849 and CHE-2108359. In addition, the authors would like to thank S. Hiemstra and C. Pfeiffer at the TTU Dept. of Chemistry and Biochemistry Machine Shop for technical support. K.F. would like to acknowledge the ACS Division of Analytical Chemistry for its graduate fellowship support sponsored by the SACP.

6. References

1. M. Cruz-Alonso, A. Lores-Padín, E. Valencia, H. González-Iglesias, B. Fernández and R. Pereiro, *Analytical and Bioanalytical Chemistry*, 2019, **411**, 549-558.
2. G. Gamez and K. Finch, *Spectrochim. Acta B*, 2018, **148**, 129-136.
3. D. Hartnell, W. Andrews, N. Smith, H. Jiang, E. McAllum, R. Rajan, F. Colbourne, M. Fitzgerald, V. Lam, R. Takechi, M. J. Pushie, M. E. Kelly and M. J. Hackett, *Front. Neurosci.*, 2020, **13**.
4. A. Limbeck, L. Brunnbauer, H. Lohninger, P. Pořízka, P. Modlitbová, J. Kaiser, P. Janovszky, A. Kéri and G. Galbács, *Anal. Chim. Acta*, 2021, **1147**, 72-98.
5. E. J. McAllum and D. J. Hare, *Spectrochim. Acta B*, 2019, **156**, 20-32.
6. G. Qian, Y. Li and A. R. Gerson, *Surf Sci Rep*, 2015, **70**, 86-133.
7. A. van der Ent, W. J. Przybyłowicz, M. D. de Jonge, H. H. Harris, C. G. Ryan, G. Tylko, D. J. Paterson, A. D. Barnabas, P. M. Kopittke and J. Mesjasz-Przybyłowicz, *New Phytol.*, 2018, **218**, 432-452.
8. M. R. Webb, V. Hoffmann and G. M. Hieftje, *Spectrochim. Acta B*, 2006, **61**, 1279-1284.
9. G. Gamez, S. Ray, F. Andrade, M. Webb and G. Hieftje, *Anal. Chem.*, 2007, **79**, 1317-1326.
10. G. Gamez, D. Frey and J. Michler, *J. Anal. Atom. Spectrom.*, 2012, **27**, 50-55.
11. G. Gamez, G. Mohanty and J. Michler, *J. Anal. Atom. Spectrom.*, 2013, **28**, 1016-1023.
12. G. Gamez, G. Mohanty and J. Michler, *J. Anal. At. Spectrom.*, 2014, **29**, 315-323.
13. M. Kroschok, J. Usala, T. Adesso and G. Gamez, *J. Anal. At. Spectrom.*, 2016, **31**, 163-170.
14. A. P. Storey, S. J. Ray, V. Hoffmann, M. Voronov, C. Engelhard, W. Buscher and G. M. Hieftje, *Appl. Spectrosc.*, 2017, **71**, 1280-1288.
15. M. Voronov, V. Hoffmann, T. Wallendorf, S. Marke, J. Mönch, C. Engelhard, W. Buscher, S. J. Ray and G. M. Hieftje, *J. Anal. At. Spectrom.*, 2012, **27**, 419-425.
16. G. Gamez, M. Voronov, S. Ray, V. Hoffmann, G. Hieftje and J. Michler, *Spectrochim. Acta B*, 2012, **70**, 1-9.
17. G. Gamez, *J. Anal. At. Spectrom.*, 2016, **31**, 2165-2174.
18. M. Rani, S. B. Dhok and R. B. Deshmukh, *IEEE Access*, 2018, **6**, 4875-4894.
19. G. R. Arce, D. J. Brady, L. Carin, H. Arguello and D. S. Kittle, *IEEE Signal Process Mag*, 2014, **31**, 105-115.
20. R. G. Baraniuk, *IEEE Signal Process Mag*, 2007, **24**, 118-120+124.

- 1
 - 2
 - 3
 - 4
 - 5
 - 6
 - 7
 - 8
 - 9
 - 10
 - 11
 - 12
 - 13
 - 14
 - 15
 - 16
 - 17
 - 18
 - 19
 - 20
 - 21
 - 22
 - 23
 - 24
 - 25
 - 26
 - 27
 - 28
 - 29
 - 30
 - 31
 - 32
 - 33
 - 34
 - 35
 - 36
 - 37
 - 38
 - 39
 - 40
 - 41
 - 42
 - 43
 - 44
 - 45
 - 46
 - 47
 - 48
 - 49
 - 50
 - 51
 - 52
 - 53
 - 54
 - 55
 - 56
 - 57
 - 58
 - 59
 - 60
21. K. Bryan and T. Leise, *SIAM Rev*, 2013, **55**, 547-566.
22. E. J. Candès, J. Romberg and T. Tao, *IEEE Trans. Inf. Theory*, 2006, **52**, 489-509.
23. E. J. Candès, J. K. Romberg and T. Tao, *Commun. Pure Appl. Math.*, 2006, **59**, 1207-1223.
24. D. L. Donoho, *IEEE Trans. Inf. Theory*, 2006, **52**, 1289-1306.
25. B. Hayes, *Am. Sci.*, 2009, **97**, 276-280.
26. D. J. Holland and L. F. Gladden, *Angew. Chem. Int. Ed.*, 2014, **53**, 13330-13340.
27. R. M. Willet, R. F. Mareia and J. M. Nichols, *Opt Eng*, 2011, **50**.
28. J. D. Usala, A. Maag, T. Nelis and G. Gamez, *J. Anal. At. Spectrom.*, 2016, **31**, 2198-2206.
29. X. Cai, B. Hu, T. Sun, K. F. Kelly and S. Baldelli, *J Chem Phys*, 2011, **135**.
30. P. Duan, Y. Wang, D. Xu, C. Yan, Z. Yang, W. Xu, W. Shi and J. Yao, *Appl. Opt.*, 2016, **55**, 3670-3675.
31. M. F. Duarte, M. A. Davenport, D. Takbar, J. N. Laska, T. Sun, K. F. Kelly and R. G. Baraniuk, *IEEE Signal Process Mag*, 2008, **25**, 83-91.
32. J. Greenberg, K. Krishnamurthy and D. Brady, *Opt. Lett.*, 2014, **39**, 111-114.
33. V. Studera, J. Bobin, M. Chahida, H. S. Mousavia, E. Candes and M. Dahane, *Proc. Natl. Acad. Sci. U. S. A.*, 2012, **109**, E1679-E1687.
34. D. Takhar, J. N. Laska, M. B. Wakin, M. F. Duarte, D. Baron, S. Sarvotham, K. F. Kelly and R. G. Baraniuk, *Proc. SPIE Int. Soc. Opt. Eng.*, 2006, **6065**.
35. J. A. Tropp and S. J. Wright, *Proc. IEEE*, 2010, **98**, 948-958.
36. J. M. Bioucas-Dias and M. A. T. Figueiredo, *IEEE Trans Image Process*, 2007, **16**, 2992-3004.
37. M. A. T. Figueiredo, R. D. Nowak and S. J. Wright, *IEEE J. Sel. Top. Sign. Proces.*, 2007, **1**, 586-597.
38. Z. Wang and A. C. Bovik, *IEEE Signal Process Mag*, 2009, **26**, 98-117.
39. A. K. Venkataramanan, C. Wu, A. C. Bovik, I. Katsavounidis and Z. Shahid, *IEEE Access*, 2021, **9**, 28872-28896.
40. K. L. Williams, G. C. Y. Chan and S. J. Ray, *Spectrochim. Acta B*, 2021, **179**.
41. A. Wagadarikar, R. John, R. Willett and D. Brady, *Appl. Opt.*, 2008, **47**, B44-B51.